Dislocation core structures in Ni-based superalloys computed using a density functional theory based flexible boundary condition approach

Anne Marie Z. Tan,[1,2] Christopher Woodward,[3,*] and Dallas R. Trinkle[1,†]

[1]*Department of Materials Science and Engineering, University of Illinois at Urbana–Champaign, Urbana, Illinois 61801, USA*

[2]*Department of Materials Science and Engineering, University of Florida, Gainesville, Florida 32611, USA*

[3]*Materials and Manufacturing Directorate, Air Force Research Laboratory, Wright Patterson Air Force Base, Dayton, Ohio 45433-7817, USA*

(Received 8 June 2018; revised manuscript received 15 February 2019; published 28 March 2019)

Nickel-based superalloys are widely used in applications requiring high strength and creep and fatigue resistance at elevated temperatures. Such structural properties are controlled by the glide and cross-slip of screw dislocations in the Ni matrix and Ni_3Al precipitates. The strengthening mechanisms are determined in turn by screw dislocation core structures that are difficult to image with weak-beam transmission electron microscopy. Core structures of two primary superalloy deformation modes, $1/2\langle 110\rangle$ Ni screw and $\langle 110\rangle$ Ni_3Al screw superdislocation, are predicted using density functional theory with flexible boundary conditions.

DOI: 10.1103/PhysRevMaterials.3.033609

I. INTRODUCTION

Nickel-based superalloys' high strength and creep and fatigue resistance are derived from their microstructure, which consists of a face-centered cubic (fcc) Ni matrix containing 40% to 80% volume fraction of $L1_2$ Ni_3Al precipitates [1]. The structural properties of both these phases are strongly influenced by the core structure of the active dislocation deformation modes. The cross-slip of ordinary $\frac{1}{2}\langle 110\rangle$ and $\langle 110\rangle$ superdislocations in Ni and Ni_3Al respectively affect work hardening and high-temperature strength. The $\frac{1}{2}\langle 110\rangle$-type dislocations in fcc Ni spontaneously dissociate into Shockley partials bounding an intrinsic stacking fault (ISF) to lower the total energy (cf. Fig. 1):

$$\tfrac{1}{2}[1\bar{1}0] \rightarrow \tfrac{1}{6}[2\bar{1}\bar{1}] + \mathrm{ISF} + \tfrac{1}{6}[1\bar{2}1]. \tag{1}$$

The $L1_2$ crystal structure is an ordered fcc derivative lattice in which the minority and majority species occupy the cube corners and face centers, respectively, doubling the periodicity of the crystal along the $\langle 110\rangle$ direction. Ni_3Al produces $\langle 110\rangle$-type superdislocations which dissociate into two $\frac{1}{2}\langle 110\rangle$-type superpartials bounding an antiphase boundary (APB); while the superpartials dissociate into Shockley partials bounding complex stacking faults (CSF):

$$\begin{aligned}[1\bar{1}0] &\rightarrow \tfrac{1}{2}[1\bar{1}0] + \mathrm{APB} + \tfrac{1}{2}[1\bar{1}0] \\ &\rightarrow \left(\tfrac{1}{6}[2\bar{1}\bar{1}] + \mathrm{CSF} + \tfrac{1}{6}[1\bar{2}1]\right) + \mathrm{APB} \\ &\quad + \left(\tfrac{1}{6}[2\bar{1}\bar{1}] + \mathrm{CSF} + \tfrac{1}{6}[1\bar{2}1]\right).\end{aligned} \tag{2}$$

An APB produces chemical disorder at the boundary, while a CSF combines the structural disorder of an ISF with the chemical disorder of an APB (cf. Figs. 1 and 2). Cross-slip of these superpartials leads to an increase in strength with increasing temperature (anomalous yield strength [2–4]), which is a key factor in the success of superalloys. The probability of cross-slip is controlled by the distance between the Shockley partials [5]. Accurate determination of the equilibrium core structures of Ni and Ni_3Al screw dislocations is crucial to modeling anomalous yield stress and creep mechanisms in Ni-based superalloys.

Given the importance of dislocations in superalloys, both experimental and modeling efforts have provided qualitative and quantitative information about dislocation geometry. Experimental estimates for dislocation core structures in Ni and Ni_3Al have all been based on measurements of the splitting distance of the Shockley partials for edge or mixed dislocations [6–9]. This is because the edge dislocations spread significantly wider than the screw dislocations and can therefore be more accurately resolved in weak-beam transmission electron microscopy (TEM) experiments. For Ni, with a Poisson ratio of $\approx$0.276, anisotropic elasticity theory predicts the ratio of equilibrium splitting distances is $d_{\mathrm{edge}}/d_{\mathrm{screw}} = 7/3$ [10]. The distance between the edge Shockley partials is then used to estimate the stacking fault (complex stacking fault) energy using anisotropic elasticity theory (AET). In turn the separation of the Shockley partials in the screw dislocations are estimated using this energy and AET. This creates a problem when one is trying to model the properties of a dislocation core using the experimentally measured planar fault energies. For example, the important feature for dislocation cross-slip is the distance between the Shockley partials and the stress needed to form the constricted (screw) dislocation. The stacking fault energy is only relevant if the anisotropic elastic solution precisely maps the splitting distance.

Atomistic simulations suggest that there is a systematic error between the actual core splitting distances and those predicted by AET, but this has never been explored or verified using density functional theory (DFT). The screw dislocation in Ni has been relaxed using various empirical potentials which predict a wide range of stacking fault energies and dissociation distances [11–13]. The planar fault energies in

*christopher.woodward@us.af.mil

†dtrinkle@illinois.edu

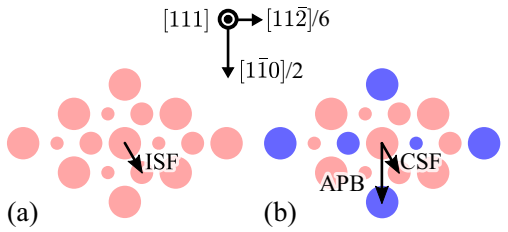

FIG. 1. The slip vectors that create (a) an ISF in fcc Ni and (b) an APB and a CSF in $L1_2$ Ni_3Al. Pink atoms represent Ni atoms and blue atoms represent Al atoms. The different atom sizes indicate atoms on different close-packed (111) planes.

Ni [14,15] and Ni_3Al [16–18] have been computed from first principles, with Schoeck *et al.* [16] and Mryasov *et al.* [17] using these energies as inputs to a Peierls-Nabarro model to compute dissociation distances in Ni_3Al, while Yu *et al.* [18] used the planar fault energies and isotropic elasticity theory to estimate these distances. While these computational studies have provided insights into active deformation mechanisms, they are at best approximations of the core structures, with limited utility in predicting the effects of variations in chemistry and kinetics. Here we assess whether the differences observed between atomistic and AET predictions for the Shockley core splitting distances are replicated in first-principles calculations of dislocation cores in Ni and Ni_3Al.

Modeling the electronic structure of an isolated dislocation is challenging due to the long-range strain field. This requires a multiscale approach that couples the core—where there are large strains—to the long-range elastic field. While anisotropic continuum elasticity theory [19,20] describes the far-field geometry around a dislocation well, the elastic solution diverges close to the core and electronic structure methods (i.e., DFT) are needed to accurately determine the dislocation core structure. Moreover, the long-range strain field of an isolated dislocation is incompatible with periodic or fixed boundary conditions which are commonly used in DFT simulations. Multiscale approaches which couple the dislocation core to finite elements [21,22], classical potentials [23,24], or flexible boundary conditions (FBC) [25] have been developed to accurately capture both the core structure as well as the long-range strain field of the dislocation by coupling the quantum mechanical core to a continuum. This work focuses on the FBC method [25], in which atoms near the dislocation core are relaxed by DFT while atoms outside the core are displaced according to the lattice Green function (LGF), effectively embedding the dislocation within an infinite harmonic bulk. Calculation of the LGF goes back to simple cubic lattices with nearest-neighbor interactions [26,27] to arbitrary Bravais lattices [28] to arbitrary crystals [29] and even a planar interface [30]. Recently, we developed a new numerical method to compute the LGF which directly accounts for the dislocation topology [31]. Here we extend our numerical method developed in Ref. [31] to compute the LGF for more complex crystal structures, including an extended fault geometry, and compute the relaxed dislocation core structures of the $\frac{1}{2}[1\bar{1}0]$ Ni screw dislocation and the $[1\bar{1}0]$ Ni_3Al superdislocation with DFT.

II. COMPUTATIONAL METHODOLOGY

A. DFT setup details

The dislocation cores in Ni and Ni_3Al are calculated using density functional theory as implemented in the Vienna *ab initio* simulation package VASP [32], which is based on plane-wave basis sets. The calculations used the Perdew-Burke-Ernzerhof generalized gradient approximation (GGA) exchange-correlation functional [33] and projector-augmented wave (PAW) potentials [34] generated by Kresse and Joubert [35] with electronic configurations of $[Ar]3d^8 4s^2$ and $[Ne]3s^2 3p^1$ to model Ni and Al. For fcc Ni, spin-polarized calculations were performed employing a plane-wave cutoff energy of 400 eV which ensures energy convergence to within 1 meV/atom. In order to facilitate rapid convergence of the Brillion zone integration, Methfessel-Paxton smearing [36] with smearing energy width of 0.25 eV was used with a $1 \times 1 \times 12$ Monkhorst-Pack k-point mesh [37]. The calculations for Ni_3Al used the spin-averaged approximation, a plane-wave cutoff energy of 337 eV, Methfessel-Paxton smearing (0.10 eV), and a $1 \times 1 \times 11$ k-point mesh.

We compute the lattice and elastic constants and planar fault energies in Ni and Ni_3Al using DFT, which we use to estimate dissociation distances from anisotropic elasticity theory for comparison with the values obtained from our relaxations. The computed lattice and elastic constants for Ni ($a_0 = 3.5219$ Å, $C_{11} = 270.4$ GPa, $C_{12} = 157.1$ GPa, $C_{44} = 129.4$ GPa) and for Ni_3Al ($a_0 = 3.5685$ Å, $C_{11} = 226.4$ GPa, $C_{12} = 153.7$ GPa, $C_{44} = 118.9$ GPa) have been previously computed and reported in Ref. [1]. We compute the planar fault energies by taking the difference in total energy per fault area between two supercells with and without the fault. For the stacking fault in Ni, we construct the faulted supercell

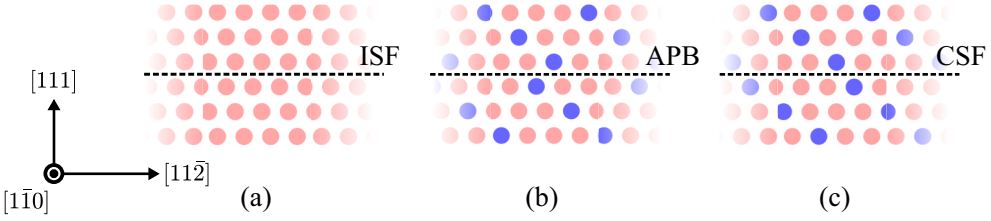

FIG. 2. Side views of (a) an ISF in fcc Ni, (b) an APB, and (c) a CSF in $L1_2$ Ni_3Al. Pink atoms represent Ni atoms and blue atoms represent Al atoms. The ISF creates structural disorder across the fault plane, the APB creates only chemical disorder, and the CSF creates both structural and chemical disorder.

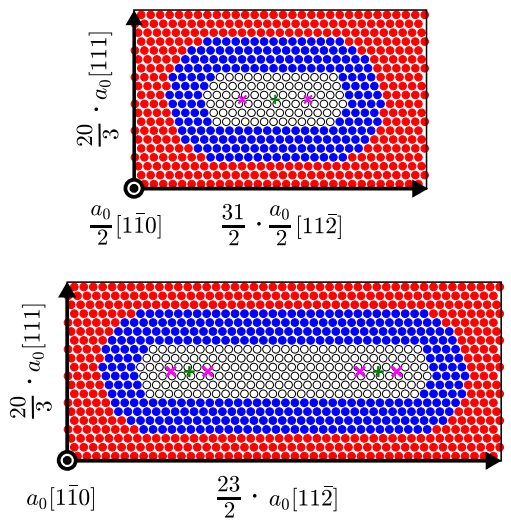

FIG. 3. DFT supercells for the (top) fcc Ni $\frac{1}{2}[1\bar{1}0]$ screw dislocation and (bottom) $L1_2$ Ni_3Al $[1\bar{1}0]$ screw superdislocation. The atoms in each supercell are divided into three regions for applying flexible boundary conditions. For Ni_3Al, each atom pictured in the figure represents a column of two nonequivalent atoms along the $[1\bar{1}0]$ direction within the supercell. Green plus signs (+) show the initial positions of $\frac{1}{2}[1\bar{1}0]$ screw dislocation(s), and magenta crosses (×) indicate estimated Shockley partial distances from previous studies [11,17].

by shortening the periodic distance along the direction perpendicular to the fault plane from 8·[111] to (8–1/3)·[111], essentially removing a close-packed plane and thus changing the stacking order at the fault. We compute the Ni stacking fault energy γ_{ISF} using a $10 \times 1 \times 12$ k-point mesh. For the planar faults in Ni_3Al, we apply alias shear [38] to construct a single APB or CSF in $1 \times 3 \times 1$ supercells. The shear vectors required to construct an APB and a CSF are $[1\bar{1}0]/2$ and $[11\bar{2}]/6$, respectively. We compute γ_{APB} and γ_{CSF} using these sheared supercells and $4 \times 1 \times 6$ k-point meshes. The computed lattice and elastic constants and planar fault energies are used as inputs to the equations presented in the Appendix to obtain anisotropic elasticity estimates of the dissociation distances for each dislocation.

Figure 3 shows the DFT supercells used to relax a $\frac{1}{2}[1\bar{1}0]$ screw dislocation in Ni and a $[1\bar{1}0]$ screw superdislocation in Ni_3Al, respectively. Supercells are constructed with fractional supercell vectors rather than the typical integer multiples of lattice vectors in order to partially cancel the stacking faults formed at the supercell boundaries due to the screw dislocation and to minimize the disruption to the charge density at the boundaries [39]. The atoms in each supercell are divided into three racetrack-shaped regions (Fig. 3). The interior (Region 1) contains atoms closest to the partial dislocations and planar fault(s). A single $\frac{1}{2}[1\bar{1}0]$ screw dislocation is introduced in the center of Region 1 [Fig. 3(a)] using displacements from anisotropic elasticity theory. To speed up convergence of the Ni_3Al superdislocation, two $\frac{1}{2}[1\bar{1}0]$ screw superpartials ≈44 Å apart [17] were introduced into Region 1 [Fig. 3(b)]. The atoms in region 1 are then relaxed using DFT Hellmann-Feynman forces and conjugate gradients. This allows the (super)partials to dissociate, following the reactions described in Eqs. (1) and (2). The Hellmann-Feynman forces that develop in the annular region (region 2) are relatively small (i.e., linear) and are passed through the LGF to displace the atoms throughout the simulation cell [11]. Region 3 contains atoms in the supercell necessary to minimize the effect of the supercell boundaries on the atoms in regions 1 and 2. Using DFT forces on atoms in regions 1 and 2, we alternate between relaxing region 1 with conjugate gradients and displacing atoms in all three regions due to LGF displacements from forces in region 2 until forces in regions 1 and 2 are smaller than 5 meV/Å.

B. Lattice Green function computation

The LGF is computed by inversion of a large, sparse matrix of force constants that correspond to the atomic positions in the dislocation geometry [31]. The force constants—which relate the force on an atom to the displacement of any atom in the system—are short ranged and bulklike even as one approaches the core. For simple crystal structures such as fcc Ni, we have shown that the force constants between a pair of atoms in the dislocation geometry can be well approximated by the closest equivalent pair of atoms in the bulk [31].

However, the APB in the $[1\bar{1}0]$ Ni_3Al superdislocation creates pairs of atoms of different atomic species than are found in bulk, and the corresponding force constants are not defined. For example, there are only Ni–Ni and Ni–Al first-nearest neighbors in bulk, but the APB creates Al–Al first-nearest neighbors as well (cf. Fig. 2). Since we use the force constants from bulk to approximate the force constants in the dislocation geometry, we do not have force constants for such pairs of atoms, which we refer to as "antisite" pairs. Instead, we approximate these force constants by performing a constrained linear least-squares fit which enforces the symmetry of the overall force constant matrix by enforcing symmetry of the onsite terms:

$$D_{\alpha\beta}(\vec{R}_i, \vec{R}_i) = D_{\beta\alpha}(\vec{R}_i, \vec{R}_i), \tag{3}$$

which gives three constraint equations for each atom i with at least one "antisite" neighbor. By the sum rule, we can rewrite this as

$$-\sum_{j\neq i} D_{\alpha\beta}(\vec{R}_i, \vec{R}_j) = -\sum_{j\neq i} D_{\beta\alpha}(\vec{R}_i, \vec{R}_j), \tag{4}$$

where atoms $j \neq i$ are all the neighbors of atom i. Separating the contributions to this sum from "antisite" neighbors j_A and "bulklike" neighbors j_B and rearranging the terms, we get

$$\sum_{j_A} D_{\alpha\beta}(\vec{R}_i, \vec{R}_{j_A}) - \sum_{j_A} D_{\beta\alpha}(\vec{R}_i, \vec{R}_{j_A}) = -\sum_{j_B} D_{\alpha\beta}(\vec{R}_i, \vec{R}_{j_B}) + \sum_{j_B} D_{\beta\alpha}(\vec{R}_i, \vec{R}_{j_B}), \tag{5}$$

where the unknown force constants are all on the left-hand side of the equation. The number of unknowns is 9×(number of "antisite" pairs), which is typically much larger than the number of constraints. Therefore, we perform a linear least-squares fit to the average of the known bulk Ni_3Al force constants for each type of neighbor pair (e.g., first-nearest

neighbors, second-nearest neighbors, etc.) to find the most physical solution from among all the possible solutions that satisfy the constraints. While this is a rather rough estimate, we find that as long as these force constants are contained entirely in region 1, they have only a weak effect on the LGF for atoms in regions 2 and 3 [31].

The dislocation force-constant matrix is numerically inverted following the method developed previously [31]. The method requires setting up a large system divided into five regions: regions 1–3, which make up the DFT supercell; a buffer region; and a far-field. The far-field contains atoms far away from the core whose displacements we approximate using the bulk elastic Green function (EGF), while the buffer region contains the remaining atoms between region 3 and the far-field. Strictly speaking, this assumption is valid only for perfect bulk crystals; when a dislocation is present, the long-range behavior of the dislocation LGF is not necessarily given by the bulk EGF [40,41]. However, we have found this to be a reasonably good approximation if the distance from the center of the dislocation to the far-field atoms is large compared to the dislocation core dimensions. For the Ni $\frac{1}{2}[1\bar{1}0]$ screw dislocation we choose a buffer size of $R = 20a_0$ (≈70 Å), while for the Ni_3Al $[1\bar{1}0]$ screw superdislocation—since the initial dislocation geometry has an extended size of ≈44 Å—we choose a larger system size of $R = 40a_0$ (≈143 Å) for computing the LGF. We verify that the errors in the LGF computation due to the far-field approximation are on the order of 10^{-4} Å^2/eV or less. We compute the LGF for forces in region 2 by applying a unit force on an atom in region 2, evaluating the resulting far-field displacements based on the EGF, determining the forces these displacements generate in the buffer region, and then solving for the displacements corresponding to the initial force by numerically inverting the force-constant matrix. This gives us one column of the LGF; by systematically looping through every atom in region 2, we can compute the required portion of the LGF matrix that gives displacements in regions 1–3 due to forces in region 2.

III. RESULTS

Figure 4 shows that the $\frac{1}{2}[1\bar{1}0]$ screw dislocation in Ni dissociates into two Shockley partials. Differential displacement (DD) maps [42] and Nye tensor distributions [43] are overlaid [44] for the screw components (top figure) and edge components (bottom figure) of the relaxed screw dislocation. The partial cores are well separated from Region 2, indicating good convergence. Estimated $d_{ISF} = 12.0$ Å is 40% larger than the 8.6 Å separation estimated from anisotropic elasticity theory using DFT-computed elastic constants and intrinsic stacking fault energy [1] (see the Appendix).

Table I compares the Ni intrinsic stacking fault energy γ_{ISF} and dissociation distance d_{ISF} to other computational studies and experiments, where we see a consistent difference between d_{ISF} direct from atomistic simulations versus the elastic estimate. Our computed γ_{ISF} of 123.6 mJ/m^2 is in good agreement with other DFT-computed values reported in the literature [14,15]. This is the first work to report the first-principles assessment of the Ni screw dislocation core

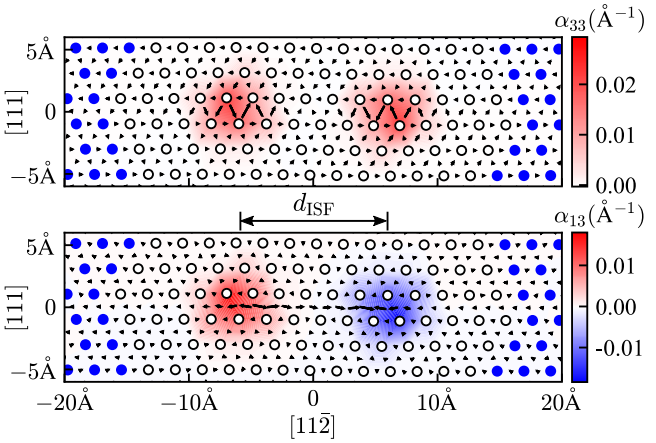

FIG. 4. Combined differential displacement and Nye tensor distribution plots for the (top) screw and (bottom) edge components of the relaxed fcc Ni $\frac{1}{2}[1\bar{1}0]$ screw dislocation. These plots show all the atoms in region 1 (white atoms) and a few atoms from region 2 (blue atoms). The edge displacements in the bottom plot are scaled by a factor of 10 to be visible compared with the screw components in the top plot. We estimate $d_{ISF} = 12.0$ Å.

structure, although there have been a number of studies which relaxed the dislocation using empirical potentials [11–13]. While empirical potentials predict a wide range of γ_{ISF} and d_{ISF}, they all produce d_{ISF} from atomistic relaxation that is 28–73% larger than the corresponding elastic estimate. The wide range of empirical potential predictions highlights the need for accurate first-principles calculations. Our computed γ_{ISF} is in good agreement with values extracted from experiment;

TABLE I. Comparison of calculated and experimental intrinsic stacking fault energies γ_{ISF} and dissociation distances d_{ISF} for the $\frac{1}{2}[1\bar{1}0]$ screw dislocation in Ni. This work (PAW-GGA + LGF) is the first to predict a Ni screw dislocation core using DFT. We find a partial separation larger than the anisotropic elasticity theory estimate, which is consistent with empirical potential calculations. Experimental studies extracted γ_{ISF} based on the coherent twin-boundary energy (Murr [45]) or observations of dissociated edge dislocations and faulted dipoles (Carter *et al.* [6]); we compute the corresponding experimental elastic estimates for d_{ISF} using Eq. (A1) and elastic constants from Simmons and Wang [46].

	γ_{ISF}	d_{ISF} (Å)		
	(mJ/m^2)	Atomistic	P-N	Elastic
DFT:				
PAW-GGA + LGF	123.6	12.0		8.6
PAW-GGA [14]	127.2			
PAW-GGA [15]	136.2			
Empirical potential:				
EAM + LGF [11]	58	19.5		15.2
EAM + LGF [11]	119	13.0		7.5
EAM [12]	176		7.4	
Finnis-Sinclair [13]	40	25.0		15.25
Experiment:				
Bright-field TEM [45]	128			7.1
Weak-beam TEM [6]	120–130			7.0–7.6

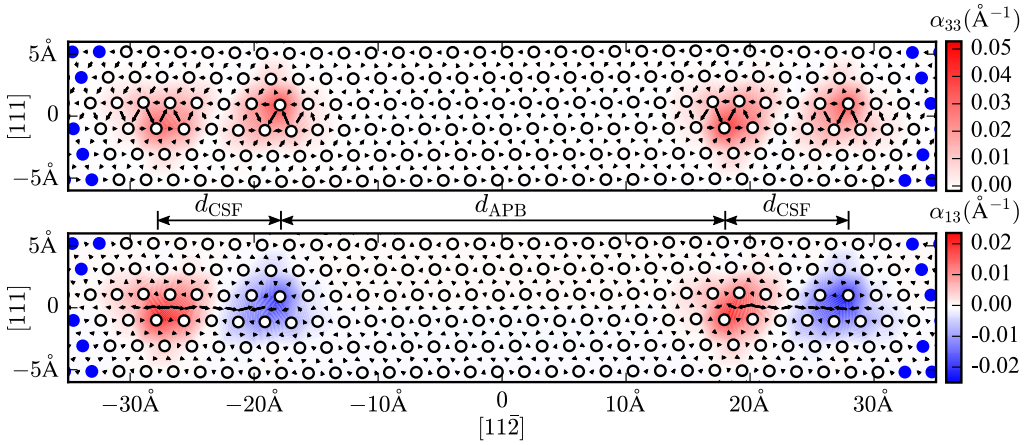

FIG. 5. Combined differential displacement and Nye tensor distribution plots for the (top) screw and (bottom) edge components of the relaxed $L1_2$ Ni_3Al $[1\bar{1}0]$ screw superdislocation. As there are two layers of atoms within the slab, we compute the differential displacements and Nye tensor as averages through the slab thickness. These plots show all the atoms in region 1 (white atoms) and a few atoms from region 2 (blue atoms). The edge displacements in the bottom plot are scaled by a factor of 10 to be visible compared with the screw components in the top plot. We estimate $d_{\text{APB}} = 36.4$ Å and $d_{\text{CSF}} = 10.0$ Å.

however, there are no direct observations of the dissociated screw dislocation in Ni with which to compare our results. Murr [45] estimated γ_{ISF} based on its relationship to the coherent twin-boundary energy, while Carter *et al.* estimated it based on observations of dissociated edge dislocations and faulted dipoles. It should also be noted that the stacking fault energy has some temperature dependence [47], where it is estimated to decrease by less than 10% from 0 K to 300 K. We compute the corresponding experimental elastic estimates for d_{ISF} listed in the table using Eq. (A1) and elastic constants from Simmons and Wang [46].

Figure 5 shows that the $[1\bar{1}0]$ screw superdislocation in Ni_3Al dissociates into two pairs of Shockley partials, where the APB and CSF are formed between the partials as expected by Eq. (2). Similarly to Fig. 4, the DD maps and Nye tensor distributions are overlaid for the screw components (top figure) and edge components (bottom figure) of the relaxed screw superdislocation [44]. Again, all the Shockley partials have the same screw components and alternating edge components with an estimated partial core splitting of $d_{\text{APB}} = 36.4$ Å and $d_{\text{CSF}} = 10.0$ Å, while $d_{\text{APB}} = 32.8$ Å and $d_{\text{CSF}} = 6.4$ Å from anisotropic elasticity theory and DFT-computed elastic constants [1] (see the Appendix). Anisotropic elasticity underestimates both d_{APB} and d_{CSF} by 3.6 Å, similar to the discrepancy between the computed and estimated values of d_{ISF} for the Ni screw dislocation.

Table II compares the dissociation distances d_{APB} and d_{CSF} computed in this work—the first first-principles assessment of the Ni_3Al screw superdislocation core structure—to other computational studies and experiments. Due to the complex extended dislocation structure, such calculations are extremely challenging and computationally expensive. FBC supercell requires 1840 atoms; without FBC, even larger supercells would be required to accurately compute the dislocation structure, making the problem intractable. Our dissociation distances are in generally good agreement with those computed by previous studies using Peierls-Nabarro model [16,17] or elasticity theory [18]. However, the key advantage of our approach compared to these continuum models is we have the atomic-level details of the core geometry that can be used to predict how different chemical species will interact with these dislocation cores. These atomic scale interactions have been shown to be critical in understanding the effects of chemistry on plastic deformation [52,53]. We note that the planar configuration studied in this work is only one possible configuration that the extended superdislocation can take. We have focused on this configuration because early computational studies based on elastic models and classical potentials predicted that the planar configuration is the most energetically stable compared to nonplanar and mixed configurations [50,51,54]. Other configurations may be of interest for consideration in future work and could also be treated with the method described in this work, given slightly different initial conditions.

IV. DISCUSSION

In both cases explored in this work the Shockley partial splitting distance was observed to be larger than that expected from anisotropic elasticity theory. Also, as shown in Tables I and II, atomistic calculations reproduce this effect across a wide range of potentials. The results presented here suggest that the conventional application of anisotropic elasticity theory produces a systematic error that should be considered when developing models for cross-slip.

Analysis of our relaxed dislocation geometries reveal that the maximum edge displacement achieved in each of the Shockley partials is in fact only about 2/3 of the expected edge component. The edge components in the Shockley partials can be calculated from the atomic positions in the relaxed dislocation cores. In the Ni $\frac{1}{2}[1\bar{1}0]$ screw dislocation, the expected edge component is $\frac{\sqrt{6}}{12}a_0 = 0.719$ Å, but the maximum edge displacement is only 0.487 Å or 67.7% of the expected edge component. Similarly, in the Ni_3Al $[1\bar{1}0]$ screw superdislocation, the expected edge component is $\frac{\sqrt{6}}{12}a_0 = 0.728$ Å,

TABLE II. Comparison of calculated and experimental planar fault energies γ_{APB} and γ_{CSF} and dissociation distances d_{APB} and d_{CSF} for the $[1\bar{1}0]$ screw superdislocation in Ni_3Al. This work (PAW-GGA + LGF) produces separations larger than estimated from anisotropic elasticity theory. While Schoeck *et al.* [16], Mryasov *et al.* [17], and Yu *et al.* [18] computed the planar fault energies with DFT, Schoeck *et al.* and Mryasov *et al.* computed d_{APB} and d_{CSF} using a Peierls-Nabarro model, while Yu *et al.* simply estimated these distances from isotropic elasticity theory. We also compute d_{APB} and d_{CSF} using the Mishin EAM potential [48]. The experimental studies (Hemker *et al.* [7], Karnthaler *et al.* [8], and Kruml *et al.* [9]) estimated γ_{APB} and γ_{CSF} based on observations of dissociated edge or mixed dislocations; we compute the corresponding screw dislocation dissociation distances d_{APB} and d_{CSF} using Eqs. (A4) and (A5) and elastic constants from Prikhodko *et al.* [49].

	γ_{APB}	γ_{CSF}	d_{APB} (Å)			d_{CSF} (Å)		
	(mJ/m^2)	(mJ/m^2)	Atomistic	P-N	Elastic	Atomistic	P-N	Elastic
DFT:								
PAW-GGA + LGF	171.2	202.4	36.4		32.8	10.0		6.4
LAPW-LDA [16]	172	223		33			6.25	
LMTO-LDA [17]	210	225		34.3 ± 8	36.0		8.7 ± 1	5.3
PAW-GGA [18]	178.76	202.32			36.01			8.76
Empirical potential:								
EAM	252	202	19		19.9	12		10.0
EAM [50]	142	121	$60 - d_{CSF}$		41.7	$60 - d_{APB}$		18.3
EAM [51]	156	259	$60 - d_{CSF}$			$60 - d_{APB}$		
Experiment:								
Weak-beam TEM [7]	180 ± 20	206 ± 30			32.1			6.8
Weak-beam TEM [8]	175 ± 15	235 ± 40			34.5			5.4
Weak-beam TEM [9]	195 ± 13	236 ± 29			30.2			5.8

but the maximum edge displacement is only 0.467 Å or 64.1% of the expected edge component. The expressions derived from AET which are used to estimate the splitting distances assume ideal splitting in which the partials achieve the full edge components; however, our results indicate that this assumption is not valid and is the likely reason for the systematic discrepancy between AET estimates and results from atomistic simulations. Reevaluating the elastic estimates using Eqs. (A1), (A4), and (A5) and the reduced edge components, we find $d^{el}_{ISF} = 13.2$ Å and $d^{el}_{CSF} = 10.3$ Å, which are in better agreement with our DFT-computed dissociation distances.

The error in estimated dissociation distances introduced by employing AET based on the idealized dissociated dislocations could lead to significant errors when modeling cross-slip mechanisms in Ni superalloys. In Ni we can estimate the scale of the error introduced by employing the anisotropic elastic mapping between our DFT-computed stacking fault energy (γ^{DFT}_{ISF}) and Shockley splitting distances obtained from relaxation with GGA-LGF (d^{DFT}_{ISF}). We can derive an effective Escaig stress, showing the effect of using the classical anisotropic theory,

$$\gamma^{DFT}_{ISF} d^{DFT}_{ISF} = \left(\gamma^{DFT}_{ISF} + \sigma_E b_e\right) d^{el}_{ISF}. \quad (6)$$

On the left are the DFT-computed values, and on the right an Escaig stress σ_E acting on the edge components b_e of the screw Shockley partials is added to the DFT-computed stacking fault energy and multiplied by the splitting distance derived using AET. Using $\gamma^{DFT}_{ISF} = 123.6$ mJ/m^2, $d^{DFT}_{ISF} = 12$ Å, $d^{el}_{ISF} = 8.6$ Å gives an effective Escaig stress of 670 MPa. Following Kang, Yin, and Cai [55], applying this Escaig stress changes the activation energy for cross-slip in Ni from 2.25 to 1.25 eV. Thus the stress (or temperature) required to enable cross-slip is decreased by approximately 50% using the first-principles observations. A similar argument holds for the anomalous yield stress; the corresponding equations for estimating the Escaig stress in Ni_3Al are

$$\left(\gamma^{DFT}_{CSF} - \gamma^{DFT}_{APB}/2\right) d^{DFT}_{CSF} = \left(\gamma^{DFT}_{CSF} - \gamma^{DFT}_{APB}/2 + \sigma_E b_e\right) d^{el}_{CSF}. \quad (7)$$

Using the values from Table II, the effective Escaig stress introduced using the anisotropic model of Shockley partial spreading is ≈900 MPa. Thus the effects are large on the scale of the stresses required to close the Shockley partial splitting distances to permit cross-slip.

It is important for the materials community to have reliable representation of the screw dislocations in engineering alloys in order to accurately model cross-slip. Cross-slip can influence work hardening through muliplication processes, and in ordered intermetallics, such as Ni_3Al, cross-slip can produce anomalous yield stress at elevated temperatures. Recently Kang, Yin, and Cai have shown using atomistic potentials that the energy barrier for cross-slip in Ni is strongly dependent on (Escaig) stresses that act on the edge components of the Shockley partials and affect the partial core splitting distance [55]. Similarly, the anomalous yield stress behavior observed in Ni_3Al is controlled by the cross-slip of superdislocations from (111) to (100) glide planes. In this case the Shockley partials that are required to constrict to form a screw (super)partial bracket a complex stacking fault. Our results imply that by using anisotropic elasticity theory to map the splitting distance to a planar fault energy introduces an effective Escaig stress which will bias analytical models of cross-slip. Therefore a more accurate method of determining the core structures and dissociation distances of these dislocations—such as has been presented in this work—is crucial in order to accurately model cross-slip mechanisms in Ni-based superalloys.

V. CONCLUSION

Core structures of screw dislocations in Ni and Ni_3Al are predicted using a DFT-based flexible boundary condition approach. Differences between predicted dissociation distances and those estimated from Peierls-Nabarro models or elasticity theory demonstrate the limitations of these continuum models and highlight the need for accurate atomistic calculations. The calculated atomic-level details of the core geometry are required for further studies of solid solution or diffusion near or along a dislocation. The computed dissociation distances can also be used to parametrize higher-length-scale models to study the anomalous yield stress and creep mechanisms in Ni-based superalloys. The current extension of the FBC approach enables calculations for a wide variety of extended dislocation cores and can be applied to dislocations in a range of technologically important materials including metals, ordered intermetallics, and semiconductors.

ACKNOWLEDGMENTS

This research was supported by NSF/DMR Grant No. 1410596 and a grant of computer time from the DOD High Performance Computing Modernization Program at the Air Force Research Laboratory Major Shared Resource Center.

APPENDIX A: ESTIMATING DISSOCIATION DISTANCES FROM ELASTICITY THEORY

We compute the dissociation distances for each dislocation from anisotropic elasticity theory in order to compare against the values obtained from our relaxations. We compute the intrinsic stacking fault distance d_{ISF} in the $\frac{1}{2}[1\bar{1}0]$ Ni screw dislocation from anisotropic elasticity theory by balancing the elastic interaction between the partial dislocations against the stacking fault energy γ_{ISF}. This yields the following expression for d_{ISF}:

$$d_{\mathrm{ISF}} = \frac{K_s b_{1s} b_{2s} + K_e b_{1e} b_{2e}}{2\pi\gamma_{\mathrm{ISF}}}, \tag{A1}$$

where b_{is} and b_{ie} are the magnitudes of the screw and edge components of the Burgers vector $\vec{b}_i$ of partial dislocation i (for this dislocation, $b_{1s} = b_{2s} = \frac{1}{2}\frac{\sqrt{2}}{2}a_0$ and $b_{1e} = -b_{2e} = \frac{1}{\sqrt{12}}\frac{\sqrt{2}}{2}a_0$) and K_s and K_e are the screw and edge components of the elastic energy coefficients derived in Ref. [10],

$$K_s = (c'_{44}c'_{55})^{1/2} \tag{A2}$$

$$K_e = \frac{(\bar{c}'_{11} + c'_{12})}{3}\left\{2\left[\frac{c'_{55}(\bar{c}'_{11} - c'_{12})}{c'_{22}(\bar{c}'_{11} + c'_{12} + 2c'_{55})}\right]^{1/2} + \left[\frac{c'_{55}(\bar{c}'_{11} - c'_{12})}{c'_{11}(\bar{c}'_{11} + c'_{12} + 2c'_{55})}\right]^{1/2}\right\}, \tag{A3}$$

where the c'_{ij} are the elastic constants rotated into the [001], $\frac{1}{\sqrt{2}}[\bar{1}\bar{1}0]$, $\frac{1}{\sqrt{2}}[1\bar{1}0]$ coordinate system, and $\bar{c}'_{11} = (c'_{11}c'_{22})^{1/2}$. Following a similar approach, we compute the antiphase boundary distance d_{APB} and complex stacking fault distance d_{CSF} in Ni_3Al from anisotropic elasticity theory by balancing the elastic interactions between the partial dislocations against the relevant planar fault energies. The force balance equations for the two leftmost partials with Burgers vectors $\vec{b}_1$ and $\vec{b}_2$ are

$$\frac{K_s b_{1s} b_{2s} + K_e b_{1e} b_{2e}}{2\pi d_{\mathrm{CSF}}} + \frac{K_s b_{1s} b_{3s} + K_e b_{1e} b_{3e}}{2\pi(d_{\mathrm{CSF}} + d_{\mathrm{APB}})} + \frac{K_s b_{1s} b_{4s} + K_e b_{1e} b_{4e}}{2\pi(2d_{\mathrm{CSF}} + d_{\mathrm{APB}})} = \gamma_{\mathrm{CSF}}, \tag{A4}$$

$$-\frac{K_s b_{2s} b_{1s} + K_e b_{2e} b_{1e}}{2\pi d_{\mathrm{CSF}}} + \frac{K_s b_{2s} b_{3s} + K_e b_{2e} b_{3e}}{2\pi d_{\mathrm{APB}}} + \frac{K_s b_{2s} b_{4s} + K_e b_{2e} b_{4e}}{2\pi(d_{\mathrm{CSF}} + d_{\mathrm{APB}})} = -\gamma_{\mathrm{CSF}} + \gamma_{\mathrm{APB}}, \tag{A5}$$

where γ_{APB} and γ_{CSF} are the antiphase boundary energy and complex stacking fault energy, respectively, $b_{1s} = b_{2s} = b_{3s} = b_{4s} = \frac{1}{2}\frac{\sqrt{2}}{2}a_0$, $b_{1e} = -b_{2e} = b_{3e} = -b_{4e} = \frac{1}{\sqrt{12}}\frac{\sqrt{2}}{2}a_0$, and the expressions for the elastic energy coefficients K_s and K_e are as defined previously in Eqs. (A2) and (A3). By symmetry, the forces on the other pair of Shockley partials are equal and opposite. We solve this pair of nonlinear equations numerically to obtain the elastic estimates for d_{APB} and d_{CSF}.

[1] C. Woodward, A. van de Walle, M. Asta, and D. R. Trinkle, Acta Mater. **75**, 60 (2014).
[2] V. Paidar, D. Pope, and V. Vitek, Acta Metall. **32**, 435 (1984).
[3] D. Pope, in *Physical Metallurgy*, 4th ed. (Elsevier, Amsterdam, 1996), pp. 2075–2104.
[4] P. Veyssière and G. Saada, in *Dislocations in Solids* (Elsevier, Amsterdam, 1996), pp. 253–441.
[5] A. T. Paxton and Y. Q. Sun, Philos. Mag. A **78**, 85 (1998).
[6] C. B. Carter and S. M. Holmes, Philos. Mag. **35**, 1161 (1977).
[7] K. J. Hemker and M. J. Mills, Philos. Mag. A **68**, 305 (1993).
[8] H. P. Karnthaler, E. T. Mühlbacherand, and C. Rentenberger, Acta Mater. **44**, 547 (1996).
[9] T. Kruml, E. Conforto, B. L. Piccolo, D. Caillard, and J. L. Martin, Acta Mater. **50**, 5091 (2002).
[10] J. P. Hirth and J. Lothe, *Theory of Dislocations*, 2nd ed. (Wiley, New York, 1982).
[11] S. Rao, T. A. Parthasarathy, and C. Woodward, Philos. Mag. A **79**, 1167 (1999).
[12] P. Szelestey, M. Patriarca, and K. Kaski, Modell. Simul. Mater. Sci. Eng. **11**, 883 (2003).
[13] Y. Qi, A. Strachan, T. Cagin, and W. A. Goddard, III Mater. Sci. Eng., A **309**, 156 (2001).
[14] M. Chandran and S. K. Sondhi, J. Appl. Phys. **109**, 103525 (2011).
[15] F. Bianchini, J. R. Kermode, and A. De Vita, Modell. Simul. Mater. Sci. Eng. **24**, 045012 (2016).
[16] G. Schoeck, S. Kohlhammer, and M. Fahnle, Philos. Mag. Lett. **79**, 849 (1999).
[17] O. N. Mryasov, Y. N. Gornostyrev, M. van Schilfgaarde, and A. J. Freeman, Acta Mater. **50**, 4545 (2002).
[18] X.-X. Yu and C.-Y. Wang, Philos. Mag. **92**, 4028 (2012).
[19] A. Stroh, J. Math. Phys. **41**, 77 (1962).

[20] D. J. Bacon, D. M. Barnett, and R. O. Scattergood, Prog. Mater. Sci. **23**, 51 (1980).
[21] E. B. Tadmor, M. Ortiz, and R. Phillips, Philos. Mag. A **73**, 1529 (1996).
[22] G. Lu, E. B. Tadmor, and E. Kaxiras, Phys. Rev. B **73**, 024108 (2006).
[23] N. Choly, G. Lu, W. E, and E. Kaxiras, Phys. Rev. B **71**, 094101 (2005).
[24] Z. C. Y. Liu, G. Lu and N. Kioussis, Modell. Simul. Mater. Sci. Eng. **15**, 275 (2007).
[25] J. E. Sinclair, P. C. Gehlen, R. G. Hoagland, and J. P. Hirth, J. Appl. Phys. **49**, 3890 (1978).
[26] V. K. Tewary, Adv. Phys. **22**, 757 (1973).
[27] I. R. MacGillivray and C. A. Sholl, J. Phys. F **13**, 23 (1983).
[28] D. R. Trinkle, Phys. Rev. B **78**, 014110 (2008).
[29] J. A. Yasi and D. R. Trinkle, Phys. Rev. E **85**, 066706 (2012).
[30] M. Ghazisaeidi and D. R. Trinkle, Phys. Rev. B **82**, 064115 (2010).
[31] Anne Marie Z. Tan and D. R. Trinkle, Phys. Rev. E **94**, 023308 (2016).
[32] G. Kresse and J. Furthmüller, Phys. Rev. B **54**, 11169 (1996).
[33] J. P. Perdew, K. Burke, and M. Ernzerhof, Phys. Rev. Lett. **77**, 3865 (1996).
[34] P. E. Blöchl, Phys. Rev. B **50**, 17953 (1994).
[35] G. Kresse and D. Joubert, Phys. Rev. B **59**, 1758 (1999).
[36] M. Methfessel and A. T. Paxton, Phys. Rev. B **40**, 3616 (1989).
[37] H. J. Monkhorst and J. D. Pack, Phys. Rev. B **13**, 5188 (1976).
[38] M. Jahnátek, J. Hafner, and M. Krajčí, Phys. Rev. B **79**, 224103 (2009).
[39] C. Woodward, Mater. Sci. Eng., A **400-401**, 59 (2005).
[40] V. K. Tewary, Phys. Rev. B **69**, 094109 (2004).
[41] V. Tewary, in *Modeling, Characterization, and Production of Nanomaterials*, Woodhead Publishing Series in Electronic and Optical Materials, edited by V. K. Tewary and Y. Zhang (Woodhead Publishing, Cambridge, 2015), pp. 55–85.
[42] V. Vítek, R. C. Perrin, and D. K. Bowen, Philos. Mag. **21**, 1049 (1970).
[43] C. S. Hartley and Y. Mishin, Acta Mater. **53**, 1313 (2005).
[44] C. Woodward, D. R. Trinkle, L. G. Hector, and D. L. Olmsted, Phys. Rev. Lett. **100**, 045507 (2008).
[45] L. E. Murr, Scr. Metall. **6**, 203 (1972).
[46] G. Simmons and H. Wang, *Single Crystal Elastic Constants and Calculated Aggregate Properties: A Handbook*, 2nd ed. (MIT Press, Cambridge, MA, 1971).
[47] S. L. Shang, W. Y. Wang, Y. Wang, Y. Du, J. X. Zhang, A. D. Patel, and Z. K. Liu, J. Phys.: Condens. Matter **24**, 155402 (2012).
[48] Y. Mishin, Acta Mater. **52**, 1451 (2004).
[49] S. V. Prikhodko, H. Yang, A. J. Ardell, J. D. Carnes, and D. G. Isaak, Metall. Mater. Trans. A **30**, 2403 (1999).
[50] R. Pasianot, D. Farkas, and E. J. Savino, Scr. Metall. Mater. **24**, 1669 (1990).
[51] M. H. Yoo, M. S. Daw, and M. J. Baskes, in *Atomistic Simulation of Materials: Beyond Pair Potentials* (Springer, Boston, MA, 1989), pp. 401–410.
[52] D. R. Trinkle and C. Woodward, Science **310**, 1665 (2005).
[53] G. P. M. Leyson, W. A. Curtin, L. G. Hector Jr., and C. F. Woodward, Nat. Mater. **9**, 750 (2010).
[54] M. Yamaguchi, V. Paidar, D. P. Pope, and V. Vitek, Philos. Mag. A **45**, 867 (1982).
[55] K. Kang, J. Yin, and W. Cai, J. Mech. Phys. Solids **62**, 181 (2014).